Chemical Engineering Journal 329 (2017) 165–177

Contents lists available at ScienceDirect

Chemical Engineering Journal

journal homepage: www.elsevier.com/locate/cej

Heat removal and catalyst deactivation in a Sabatier reactor for chemical fixation of CO_2: Simulation-based analysis

Duo Sun, Faisal Mohamed Khan, David S.A. Simakov *

Department of Chemical Engineering, University of Waterloo, Waterloo, ON N2L 3G1, Canada

HIGHLIGHTS

- Sabatier reactor for CO_2 conversion is modelled considering catalyst deactivation.
- The reactor is a molten salt-cooled heat-exchanger type packed bed.
- Biogas fed reactor is analyzed numerically over the range of operating parameters.
- Feed and cooling rates are crucial parameters affecting the reactor performance.
- The model predicts CH_4 yields of 80–90% over the 10,000 time-on-stream.

GRAPHICAL ABSTRACT

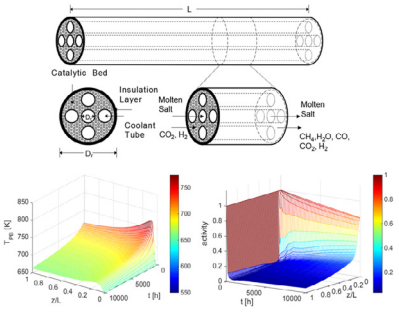

ARTICLE INFO

Article history:
Available online 28 June 2017

Keywords:
Sabatier reactor
CO_2 conversion
Packed-bed reactor
Catalyst deactivation

ABSTRACT

Thermo-catalytic hydrogenation of CO_2 into synthetic CH_4 via Sabatier reaction is an attractive route to reduce fossil fuels consumption and to limit greenhouse gas emissions, while potentially providing revenue. Hydrogen required for the reaction can be generated by water electrolysis using renewable or low carbon footprint electricity. With respect to CO_2 methanation, a number of technological challenges have to be resolved in order to make this technology economically viable. The highly exothermic nature of the Sabatier reaction makes heat removal a challenging task. Another major problem is catalyst deactivation by coking caused by CH_4 cracking at elevated temperatures. Maximizing CH_4 production over extended periods of operation will require highly efficient heat removal to facilitate CH_4 production, while minimizing catalyst deactivation. In this study, a heat-exchanger type, molten salt-cooled packed bed reactor is analyzed using a transient mathematical model. The model considers inter-compartment heat exchange and catalyst deactivation by coking, assuming the use of a Ni/Al_2O_3 catalyst. The reactor performance was investigated in terms of CO_2 conversion and CH_4 yield for the case of the feed containing CO_2 and H_2, and for the case of the reactor fed with biogas (40% CO_2 and 60% CH_4) and H_2. The model predicts that, though the catalyst deactivation leads to a substantial decline in the reactor performance, CH_4 yields and CO_2 conversions over 80% are achievable after 10,000 h of operation.

1. Introduction

The increasing levels of global CO_2 emissions have prompted research in utilizing CO_2 as a feedstock for generating synthetic fuels and chemicals [1]. The current usage of CO_2 as a feedstock in industries is limited to processes such as synthesis of urea, salicylic acid and polycarbonates [1]. Conversion of CO_2 into synthetic CH_4 via methanation, also called the Sabatier reaction, has recently gained increasing interest as a process being more advantageous thermodynamically as compared to other reactions which form higher hydrocarbons or alcohols [2].

* Corresponding author.
E-mail address: dsimakov@uwaterloo.ca (D.S.A. Simakov).

http://dx.doi.org/10.1016/j.cej.2017.06.160
1385-8947/

Nomenclature

a	activity factor
$a_{c,HE}$	cooling tube surface-to-volume ratio, m^{-1}
$a_{r,HE}$	cooling tube surface-to-packed volume ratio, m^{-1}
$a_{r,HL}$	reactor surface-to-volume ratio, m^{-1}
A_c	total cross-sectional area of cooling tubes, m^2
A_j	pre-exponential factor of the rate coefficient of reaction j, units of k_j
B_j	pre-exponential factor of the adsorption coefficient of species i, units of K_j
C_i	molar concentration of species i, mol/m^3
C_t	total molar concentration, mol/m^3
C_{pc}	coolant heat capacity, kJ/(kg K)
C_{pg}	gas heat capacity, kJ/(mol K)
d	wall thickness, m
d_p	catalytic pellet diameter, m
D	diameter, m
D_{ae}	effective axial diffusion coefficient, m^2/s
D_m	gas molecular diffusivity, m^2/s
E_j	activation energy of reaction j, kJ/mol
G	gravimetric (mass) flow rate, kg/s
h_{nc}	natural heat convection coefficient, $kJ/(m^2\ s\ K)$
h_w	effective wall heat transfer coefficient, $kJ/(m^2\ s\ K)$
ΔH_i	adsorption enthalpy change of species i, kJ/mol
k_{ae}	effective axial thermal conductivity, kJ/(m s K)
k_j	rate constant of reaction j
K_i	adsorption constant of species i, bar^{-1}
$K_{j,eq}$	equilibrium constant of reaction j
L	reactor length, m
Nu	Nusselt number
p_i	partial pressure of gaseous species i, bar
P	reactor pressure, bar
Pr	Prandtl number
P_{tf}	total feed gas pressure, bar
Re	Reynolds number
R_j	rate of reaction j, mol/(kg s)
R_g	gas constant, kJ/(mol K)
SV	gas hourly space velocity, h^{-1}
t	time, s
T	reactor temperature, K
T_c	coolant temperature, K
T_e	environment temperature, K
U_w	effective wall heat transfer coefficient, $kJ/(m^2\ s\ K)$
v	fluid velocity, m/s
V	compartment volume, m^3
z	reactor length coordinate, m

Greek letters

ε	catalyst bed porosity
ϕ	Thiele modulus
η_j	effectiveness factor of reaction j
λ	thermal conductivity, kW/(m K)
μ	viscosity, kg/(m s)
ρ_c	coolant density, kg/m^3
ρ_g	gas molar density, mol/m^3
ρ_s	solid density, kg/m^3
τ_b	catalyst bed tortuosity

Subscripts

c	coolant
eff	effective
eq	equilibrium
f	feed
g	gas
HE	heat exchange
HL	heat loss
int	initial
nc	natural convection
p	packed bed
s	solid
r	reactor

The exothermic Sabatier reaction, Eq. (3), is accompanied by the mildly endothermic reverse water gas shift, Eq. (2), and the strongly exothermic CO methanation, Eq. (1).

$$CO + 3H_2 \leftrightarrow CH_4 + H_2O \quad \Delta H^\circ_{298} = -206.1\ kJ/mol \tag{1}$$

$$CO_2 + H_2 \leftrightarrow CO + H_2O \quad \Delta H^\circ_{298} = +41.2\ kJ/mol \tag{2}$$

$$CO_2 + 4H_2 \leftrightarrow CH_4 + 2H_2O \quad \Delta H^\circ_{298} = -164.9\ kJ/mol \tag{3}$$

The overall process is highly exothermic which requires efficient heat removal, in order to facilitate CH_4 production. In addition to this thermodynamic constrain, reactor overheating can also lead to fast catalyst deactivation by sintering and coking.

Methanation of CO_2 over catalysts based on various group VIII metals (e.g., Rh, Ru, Co) supported on TiO_2, SiO_2, Al_2O_3, CeO_2, and ZrO_2 has been studied as a possible method to produce synthetic natural gas [3–7]. However, Ni-based catalysts have typically been used in commercial processes due to the low costs, high activity and good selectivity to CH_4 formation [1,8]. Despite the abovementioned advantages, the implementation of Ni-based catalysts for CO_2 methanation is limited because of high tendency to deactivation by poisoning, coking and sintering [9]. Poisoning of Ni catalysts typically occurs due to the presence of sulphur compounds in the feed gas stream. [9,10]. Sintering also plays an important role in the deactivation of Ni-based catalysts. Studies have indicated that Ni sintering proceeds by chemical sintering, via the formation of $Ni(CO)_4$ [11].

While operating at relatively low temperatures typically employed in CO_2 methanation (700–800 K) and in the absence of sulphur (can be removed from feed gas by adsorbents), catalytic activity of Ni is mainly reduced by coking. Carbon deposition deactivates the catalyst by fouling the catalyst surface, blocking catalyst pores and disintegrating the catalyst support [9]. The three major forms of carbon deposited on Ni catalysts are encapsulating hydrocarbons films formed by polymerization at temperatures below 750 K, whiskerlike carbon formed at temperatures higher than 725 K, and pyrolytic carbon formed by cracking of hydrocarbons above 875 K [9]. The most thermodynamically probable reactions involved in carbon deposition in the methanation process are CH_4 cracking, Eq. (4), Boudouard reaction, Eq. (5), and CO reduction (reverse gasification), Eq. (6) [12]:

$$CH_4 \leftrightarrow C + 2H_2 \quad \Delta H^\circ_{298} = +74.8\ kJ/mol \tag{4}$$

$$2CO \leftrightarrow C + CO_2 \quad \Delta H^\circ_{298} = -173.3\ kJ/mol \tag{5}$$

$$CO + H_2 \leftrightarrow C + H_2O \quad \Delta H^\circ_{298} = -131.3\ kJ/mol \tag{6}$$

Deactivation of Ni-based catalyst by coking has been studied by various researchers and our understanding of the carbon formation mechanisms is relatively complete. Claridge et al. investigated the effect of temperature on the rate of carbon deposition by the Boudouard reaction and CH_4 cracking reaction. Their results indicated that carbon deposition by CH_4 cracking dominates at relatively high temperatures, while carbon formation via Boudouard reaction mainly occurs at lower temperatures, with both process contributing equally to carbon formation at 890 K [13].

Other studies investigated the effect of various feed conditions on the Boudouard reaction showing that low CO partial pressures, high H_2/CO ratios, and high partial pressures of CO_2 reduce the carbon formation rate via the CO disproportionation. These findings indicate that the major cause of coking in the CO_2 methanation process is CH_4 cracking [14,15]. Analysis of the reaction mechanisms involved in carbon deposition via CH_4 cracking indicated that the rate-limiting step is the dissociative adsorption of CH_4 on the catalyst with H_2 adsorption acting in competition. The rate of the reaction was found to be a function of temperature and partial pressure of H_2 and CH_4. It is worth mentioning that CH_4 cracking on Ni surfaces can be used to generate carbon nanotubes and H_2 [16], with the coking threshold directly related to the size of Ni nanocrystallites [17].

The goal of the present study was to analyze the effect of the Ni-based catalyst deactivation via CH_4 cracking on reactor performance under various operating conditions including space velocity, pressure, and cooling rate. A heat-exchanger type, multiple-tube Sabatier reactor internally cooled by the molten salt was suggested as an effective design solution for heat removal. A transient pseudo-homogeneous mathematical model [18,19] was used to simulate the reactor performance. To simulate catalyst deactivation via CH_4 cracking, first order deactivation rate was assumed [20]. The reactor performance was analyzed over extended operating periods, up to 10,000 h time on stream, in terms of CO_2 conversion, selectivity to CH_4 formation, and CH_4 yield. Our study provide new insights into the operation of the molten salt-cooled Sabatier reactor subject to catalyst deactivation by coking. Importantly, our mathematical model accounts for temperature variations of the heat transfer fluid, as well as for the catalyst deactivation. The results of numerical simulations predict that, with the optimized heat removal, it is possible to operate the reactor over extended periods of time and with reasonably high CH_4 yields, even using the Ni-based catalyst that is susceptible to deactivation by coking.

2. Model formulation

Various reactor configurations were suggested for CO_2 methanation, including fluidized beds, slurry reactors, honeycombs, microchannel reactors, and fixed beds [21]. The Sabatier reactor design suggested in the current study is shown in Fig. 1. The reactor is a heat-exchanger type packed bed internally cooled by molten salt flowing in multiple cooling tubes. To minimize uncontrollable heat losses to the environment, the reactor is insulated by a layer of quartz wool. Both the external and internal tubes are made of stainless steel.

The dimensions used in numerical simulations are listed in Table 1. Since we used a 1D mathematical model in our study, we selected reactor dimensions in such a way that the radial heat transfer dimension is minimized. Due to the small diameter of the cooling tubes (D_c = 20 mm) and high thermal conductivity of the molten salt, significant radial gradients are not expected to develop within the molten salt [22]. In order to minimize the heat transfer distance in the packed bed, the number of cooling tubes was set to N = 13. For this number of tubes and for the dimensions described in Table 1 with evenly distributed tubes, the distance between any two adjusted cooling tubes will be 19 ± 1 mm. Thermal conductivity of the packed bed should prevent large radial gradients over that relatively small distance [23]. In general, 1D models of packed beds are believed to be capable of describing at least the qualitative trends [24].

A transient, one-dimensional, pseudo-homogeneous mathematical model [18,19] was used to simulate the reactor. The model accounts for axial mass and heat dispersion and for the temperature dependence of thermo-physical properties. Component mass balance and energy balance for the packed bed compartment are given by Eq. (7) and Eq. (8), respectively. The model accounts for temperature variations of the heat transfer fluid, as opposed to assuming constant coolant temperature [24,25]. The temperature distribution in a single molten salt tube is described by Eq. (9). Note that the energy balance for the packed bed includes the heat loss term (T_e = 298 K is the temperature of the environment) in addition to the heat exchange term.

$$\varepsilon\frac{\partial C_i}{\partial t} = D_{ae}\frac{\partial^2 C_i}{\partial z^2} - \varepsilon v_g\frac{\partial C_i}{\partial z} + a(1-\varepsilon)\rho_s\sum_j \eta_j R_{ij} \tag{7}$$

$$\begin{aligned}(\rho C_p)_{eff}\frac{\partial T}{\partial t} &= k_{ae}\frac{\partial^2 T}{\partial z^2} - \varepsilon\rho_g C_{pg} v_g\frac{\partial T}{\partial z} + \\ &+ a(1-\varepsilon)\rho_s\sum_j(-\Delta H_j)\eta_j R_j \\ &- U_{w,HE}a_{r,HE}(T-T_c) - U_{w,HL}a_{r,HL}(T-T_e)\end{aligned} \tag{8}$$

$$\rho_c C_{pc}\frac{\partial T_c}{\partial t} = \lambda_c\frac{\partial^2 T_c}{\partial z^2} - \rho_c C_{pc} v_c\frac{\partial T_c}{\partial z} - U_{w,HE}a_{c,HE}(T_c - T) \tag{9}$$

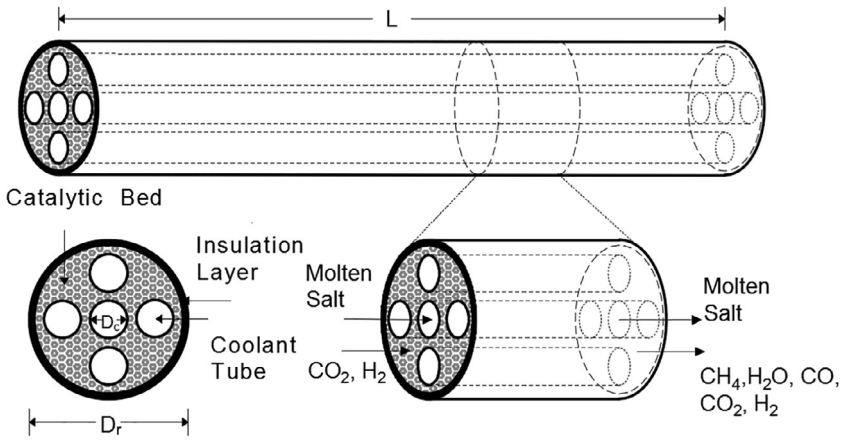

Fig. 1. Schematic of the molten salt-cooled, heat-exchanger type packed bed Sabatier reactor.

Table 1
Reactor dimensions.

D_r (m)	D_c (m)	d_w (m)	d_{iw} (m)	d_p (m)	N (m)	L (m)	V_r (m^3)	V_c (m^3)
0.2	0.02	0.002	0.05	0.003	13	1	0.0255	0.0041

D and L denote diameter and length of the packed bed (D_r) and coolant (D_c) compartments; d_w denote thickness of the reactor wall and cooling tube; d_{iw} is insulation layer thickness; V denote volume of the packed bed (V_r) and coolant compartment (V_c); N is the number of the molten salt coolant tubes; d_p is the (spherical) catalytic pellet size.

$$\begin{aligned} z=0 \quad & \varepsilon v_g(C_{i,f}-C_i) = -D_{ae}\frac{\partial C_i}{\partial z} \qquad z=L \quad \frac{\partial C_i}{\partial z}=0 \\ & \varepsilon\rho_g v_g C_{pg}(T_f-T) = -k_{ae}\frac{\partial T}{\partial z} \qquad \frac{\partial T}{\partial z}=0 \\ & \rho_c v_c C_c(T_{c,f}-T_c) = -\lambda_c\frac{\partial T_c}{\partial z} \qquad \frac{\partial T_c}{\partial z}=0 \end{aligned} \tag{10}$$

$$\begin{aligned} t=0 \quad & C_i(0,z) = C_{i,\text{int}} \\ & T(0,z) = T_{\text{int}} \\ & T_c(0,z) = T_{c,\text{int}} \end{aligned} \tag{11}$$

Pressure drop was accounted for using Ergun equation, Eq. (12). Velocity correction was calculated using Eq. (13). Effective heat capacity in Eq. (8) is defined by Eq. (14).

$$\frac{dP}{dz} = -150\frac{(1-\varepsilon)^2\mu_g}{d_p^2\varepsilon^3}v_g - 1.75\frac{(1-\varepsilon)\rho_g}{d_p\varepsilon^3}v_g^2 \tag{12}$$

$$v_g = v_{gf}\frac{C_t}{C_{t,f}} \tag{13}$$

$$(\rho C_p)_{eff} = \varepsilon\rho_g C_{pg} + (1-\varepsilon)\rho_s C_{ps} \tag{14}$$

2.1. Catalytic kinetics

Reaction rates are calculated using the commonly adopted kinetics for methane steam reforming over the Ni/Al_2O_3 catalyst [26,27], Eqs. (15a)(15c). These kinetic expressions account for the reversibility of the reforming and water gas shift reactions and can be used without modification for modeling of the CO_2 methanation reaction system, Eqs. (1)–(3). All parameters are tabulated in the literature, e.g., see Tables 3 and 4 in Rodríguez et al. (2012) [28] that include parameters for the rate constants, adsorption constants, as well as the temperature dependence of the equilibrium constants.

$$R_1 = \frac{k_1}{p_{H_2}^{2.5}}\left(p_{CH_4}p_{H_2O} - \frac{p_{H_2}^3 p_{CO}}{K_{1,eq}}\right)\frac{1}{\text{den}^2} \tag{15a}$$

$$R_2 = \frac{k_2}{p_{H_2}}\left(p_{CO}p_{H_2O} - \frac{p_{H_2}p_{CO_2}}{K_{2,eq}}\right)\frac{1}{\text{den}^2} \tag{15b}$$

$$R_3 = \frac{k_3}{p_{H_2}^{3.5}}\left(p_{CH_4}p_{H_2O}^2 - \frac{p_{H_2}p_{CO_2}}{K_{3,eq}}\right)\frac{1}{\text{den}^2} \tag{15c}$$

$$\text{den} = 1 + K_{CO}p_{CO} + K_{H_2}p_{H_2} + K_{CH_4}p_{CH_4} + \frac{K_{H_2O}p_{H_2O}}{p_{H_2}}$$

$$k_j = A_j\exp\left(\frac{-E_j}{R_gT}\right) \quad K_i = B_i\exp\left(\frac{-\Delta H_i}{R_gT}\right)$$

Estimation the intraparticle and interphase transport limitations [18] has shown that intraparticle temperature gradients and interphase transport limitations can be neglected for the size of catalytic pellets used in our simulations (d_p = 3 mm, Table 1), in the entire range of parameters studied. However, it has been found that the internal (intraparticle) diffusion resistance cannot be neglected. This limitation was accounted for using the effectiveness factor defined below (the dimensionless Thiele Modulus, ϕ_j for the reaction j, is defined with the modified reaction rate constants; the original rate constants (k_j) are given by Eq. (15)):

$$\eta_j = \frac{3}{\phi_j}\left(\frac{1}{\tanh\phi_j} - \frac{1}{\phi_j}\right) \quad \phi_j = \sqrt{\frac{\hat{k}_j d_p^2}{4D_m}}$$
$$\hat{k}_1 = \frac{k_1\rho_s(1-\varepsilon)}{\sqrt{P_{tf}}\rho_g\varepsilon} \quad \hat{k}_2 = \frac{k_2\rho_s(1-\varepsilon)P_{tf}}{\rho_g\varepsilon} \quad \hat{k}_3 = \frac{k_3\rho_s(1-\varepsilon)}{\sqrt{P_{tf}}\rho_g\varepsilon} \tag{16}$$

2.2. Catalyst deactivation kinetics

A general form of the catalyst activity factor multiplying reaction terms in Eqs. (7), (8) is written as follows:

$$-\frac{da}{dt} = r_d a^d \tag{17}$$

Assuming 1st order deactivation ($d = 1$), the following expression for the catalyst activity factor is derived by integration:

$$a = \exp(-r_d t) \tag{18}$$

As it was mentioned in the Introduction, for temperatures above 700 K low CO partial pressures, the deactivation of Ni-based catalysts is predominantly caused by the accumulation of the filamentous carbon formed via CH_4 cracking, Eq. (4). The Boudouard reaction and the CO reduction (reverse gasification), Eqs. (5), (6), require CO as a source of carbon. However, in all our simulations the amount of CO produced was less than 1 mol% (mole fraction less than 0.01). On the other hand, CH_4 concentrations obtained in our simulations were relatively high, as well as H_2 concentrations (see Figs. 2, 4, and 6), thus the carbon gasification by H_2 is expected to be significant.

The reactions of carbon gasification by H_2O and CO_2, reverse reactions in Eqs. (5), (6), can potentially occur during methanation because CO_2 is a reactant and H_2O is a product. However, these reactions are highly endothermic, as compared to the mildly exothermic carbon gasification by H_2. Both steam and CO_2 gasification are thermodynamically favorable at temperatures above 950 K, when the corresponding equilibrium constant is significantly higher than 1 [29]. On the other hand, hydrogasification (reverse reaction in Eq. (4)) is thermodynamically favorable below that temperature [29]. Since in our simulations maximum temperatures did not exceed 750 K, the H_2-induced gasification is expected to be the predominant process for carbon removal.

Consequently, the catalyst deactivation in the present study was assumed to be solely induced by CH_4 cracking, while considering the reverse reaction of gasification by H_2. The following power law rate expression was adopted from the literature [30]:

$$r_d = k_d\frac{p_{CH_4}}{p_{H_2}} \quad k_d = k_{d0}\exp\left(\frac{-E_d}{R_gT}\right) \tag{19}$$

The activation energy (E_d = 178 kJ/mol), and pre-exponential factor ($k_{d0} = 2.35\times10^{-8}\ \text{min}^{-1}$) were extracted from the experimental data available in the literature (Fig. 5 in Borghei et al. (2010) [20]). Note that these parameters are not expected to reflect exactly the rate of carbon formation under the conditions used in our simulations, as these parameters were estimated for methane cracking (in the presence of H_2), not for CO_2 methanation. However, as kinetic data on catalyst deactivation during the CO_2 methanation reaction is scarce, we selected these parameters for our

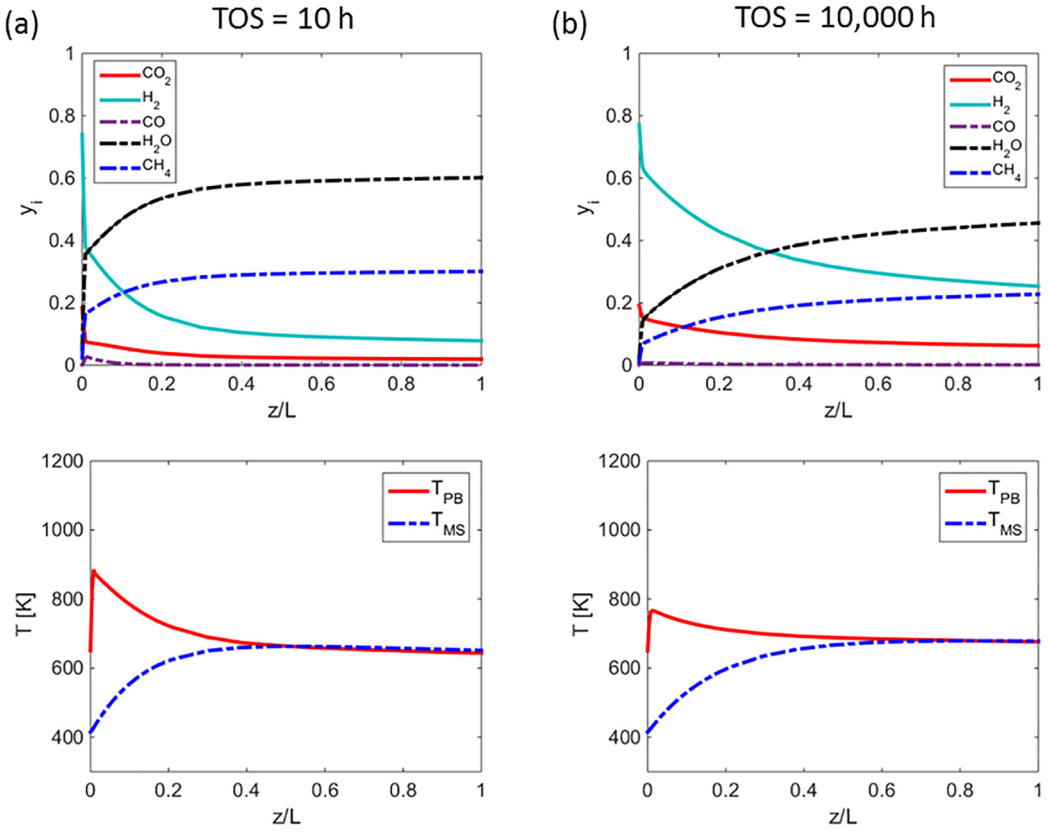

Fig. 2. Spatial profiles of mole fractions (upper panels) and temperatures (lower panel) for TOS = 10 h (a) and TOS = 10,000 h (b). T_{PB} and T_{MS} denote temperatures in the packed bed (PB) and molten salt (MS) compartments. *Parameters:* T_f = 650 K, *GHSV* = 1000 h^{-1}, P_f = 5 bar, $G_c = 0.4G_{c,0}$.

model. From the catalyst deactivation viewpoint, our study is intended for the investigation of main trends rather than exact prediction of the reactor behaviour. Still, since these are experimentally estimated kinetic parameters, the model is expected to have certain predictive ability.

2.3. Transport parameters

The effective axial mass dispersion coefficient is calculated using the following correlation [31]:

$$D_{ae} = \varepsilon\left(\frac{D_m}{\tau_b} + 0.5 d_p v_g\right) \quad \tau_b = \frac{1}{\varepsilon^{0.5}} \tag{20}$$

The expression for the effective axial heat dispersion coefficient (k_{ae}), Eq. (21), was derived from the heat conductivity correlations developed for catalytic fixed beds [19,32,33]. Values of k_{ae} were calculated using original correlations [32,33] in the relevant range of parameters, plotted versus particle Reynolds number (Re_p), and fitted using least squares analysis, resulting in the following correlation:

$$k_{ae} = \lambda_g(8 + 0.05\mathrm{Re}_p^{1.09}) \quad \mathrm{Re}_p = \frac{v_g \rho_g d_p}{\mu_g} \tag{21}$$

Wall heat transfer coefficients are determined by resistances in series, accounting for contributions of the fixed bed, molten salt, tube walls, and insulation layer, Fig. 1:

$$U_{w,HE} = \left(\frac{1}{h_{wr}} + \frac{d_w}{\lambda_w} + \frac{1}{h_{wc}}\right)^{-1} \tag{22a}$$

$$U_{w,HL} = \left(\frac{1}{h_{wr}} + \frac{d_w}{k_w} + \frac{d_{iw}}{k_{iw}} + \frac{1}{h_{nc}}\right)^{-1} \tag{22b}$$

The wall heat exchange coefficient between the catalytic bed and the coolant tube, $U_{w,HE}$, accounts for resistances of the fixed bed, the coolant tube wall, and the molten salt, Eq. (22a). Similarly, the correlation for the wall heat loss coefficient, $U_{w,HL}$, accounts for resistances through the catalytic bed, the reactor wall, and the quartz wool insulation layer [34], accounting also for heat losses from the reactor external surface via natural convection (h_{nc}) [35]. Since the insulation layer resistance and natural convection are dominant in Eq. (22b), the wall heat loss coefficient was nearly constant in all simulations: $U_{w,HL} \approx 0.01$ W/(m^2 K).

The effective wall heat transfer coefficient for the reaction compartment (h_{wr}) is estimated using the following correlation obtained in the similar way as Eq. (21), using a complete set of the original correlations [19,32,33]:

$$Nu_p = \frac{h_{wr} d_p}{\lambda_g} = 24 + 0.34 \quad \mathrm{Re}_p^{0.77}\mathrm{Re}_p = \frac{v_g \rho_g d_p}{\mu_g} \tag{23}$$

The effective wall heat transfer coefficient for the coolant tube (h_{wc}) is estimated using the following, adopted from the literature, correlations [36–38]:

$$\mathrm{Re}_c < 2030 \quad Nu_c = 3.66 + \frac{0.065\mathrm{Re}_c\mathrm{Pr}_c(D_c/L)}{1 + 0.04[\mathrm{Re}_c\mathrm{Pr}_c(D_c/L)]^{2/3}} \tag{24a}$$

$$2030 < \mathrm{Re}_c < 4000 \quad Nu_{wc} = 0.012(\mathrm{Re}_c^{0.87} - 280)\mathrm{Pr}_c^{0.4}[1 + (D_c/L)^{2/3}] \tag{24b}$$

$$\mathrm{Re}_c > 4000 \quad Nu_c = 0.027\mathrm{Re}_c^{0.8}\mathrm{Pr}_c^{1/3}$$
$$Nu_{wc} = \frac{h_{wc} D_c}{\lambda_c} \quad \mathrm{Re}_c = \frac{v_c \rho_c D_c}{\mu_c} \quad \mathrm{Pr}_c = \frac{C_{pc}\mu_c}{\lambda_c} \tag{24c}$$

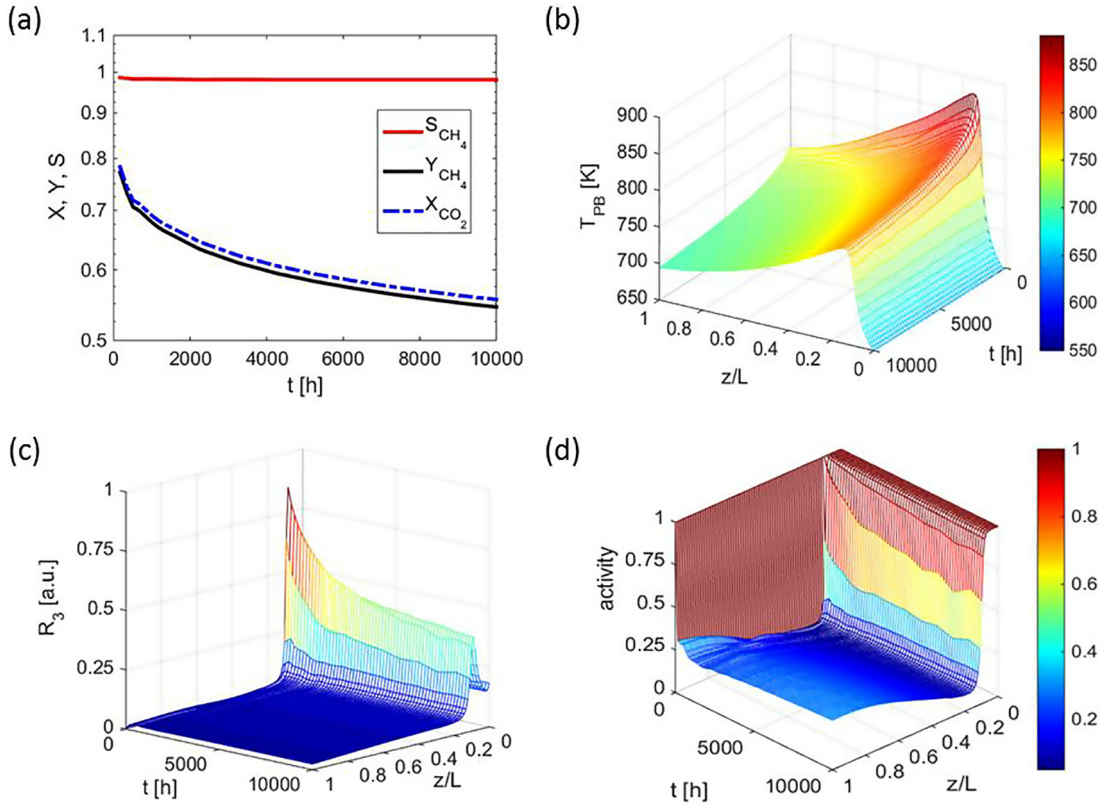

Fig. 3. Temporal evolution of the reactor performance (a) and spatiotemporal profiles of the packed bed temperature (b), Sabatier reaction rate (c), and catalyst activity (d). X_{CO_2}, S_{CH_4}, and Y_{CH_4} denote conversion, selectivity, and yield, Eqs. (25)–(27); R_3, Eq. (15c) is shown as normalized reaction rate. *Parameters:* $T_f = 650$ K, *GHSV* = 25,000 h^{-1}, $P_f = 5$ bar, $G_c = 0.4G_{c,0}$.

2.4. Numerical procedure

The model was solved using the MATLAB PDE solver with a second-order accurate spatial discretization (finite elements) based on a fixed set of user-specified nodes (100 nodes were used) and time integration done by the stiff ODE solver (ode 15s). Dependences of thermophysical properties (density, viscosity, heat capacity, diffusivity, and thermal conductivity) on temperature, pressure and composition were accounted for using polynomial regressions fitted to the data on thermophysical properties from the literature [39–41]. Molten salt properties were adopted from the data on commercially available molten salts (Dynalene, Inc. [42], Dynalene MS-2).

3. Results and discussion

The effect of catalyst deactivation and heat removal on the reactor performance is first analyzed for the case of the reactor fed with pure CO_2 and H_2. In practical applications this approach will require CO_2 separation from the carbon-rich stream such as landfill gas, biogas or flue gas. Another approach is to feed a mixed feedstock such as raw biogas, only pre-treated to remove H_2S to prevent catalyst poisoning by sulphur. In the analysis of the reactor fed with raw biogas (after sulphur removal) it is assumed that biogas contains 60% CH_4 and 40% CO_2. This case, which is more complicated than the case of pure CO_2 feed, is studied in more detail, specifically investigating the effects of space velocity, pressure, and heat removal rate on the reactor performance in terms of CH_4 yield.

The presence of CH_4 in the feed is expected to induce catalyst deactivation by coking, Eq. (19). On the other hand, the reaction system will be less exothermic as CH_4 can react with H_2O produced via methanation reactions via endothermic steam reforming reactions, Eq. (1), (3), making heat removal more efficient and decreasing the packed bed temperature. Lower reactor temperatures will result in lower rate of the catalyst deactivation, Eq. (19). Dry CH_4 reforming is not considered as it is not expected to occur to a significant extent at relatively low temperatures considered in this study, below 800 K [43].

For the case of the reactor fed with the mixture of CO_2 and H_2, the reactor performance is evaluated in terms of CO_2 conversion (X_{CO_2}), selectivity to CH_4 (S_{CH_4}), and CH_4 yield (Y_{CH_4}) which can be calculated based on molar fractions:

$$X_{CO_2} = \frac{y_{CH_4} + y_{CO}}{y_{CH_4} + y_{CO} + y_{CO_2}} \tag{25}$$

$$S_{CH_4} = \frac{y_{CH_4}}{y_{CH_4} + y_{CO}} \tag{26}$$

$$Y_{CH_4} = \frac{y_{CH_4}}{y_{CH_4} + y_{CO} + y_{CO_2}} \tag{27}$$

For the case of the reactor fed with biogas, since the inlet mixture already contains CH_4 it is more convenient to evaluate the reactor performance solely in terms of CH_4 produced from CO_2. The following equation (based on molar rates) was used to calculate the yield of CH_4 for the case of the biogas-fed reactor:

$$Y_{CH_4} = \frac{F_{CH_4,out} - F_{CH_4,in}}{F_{CO_2,in}} \tag{27a}$$

In all simulations, the initial temperatures (Eq. (11), T_{int}, $T_{c,int}$) were set to 550 K. The molten salt feed temperature was set to its minimum operating temperature of 415 K [42]. The feed molar

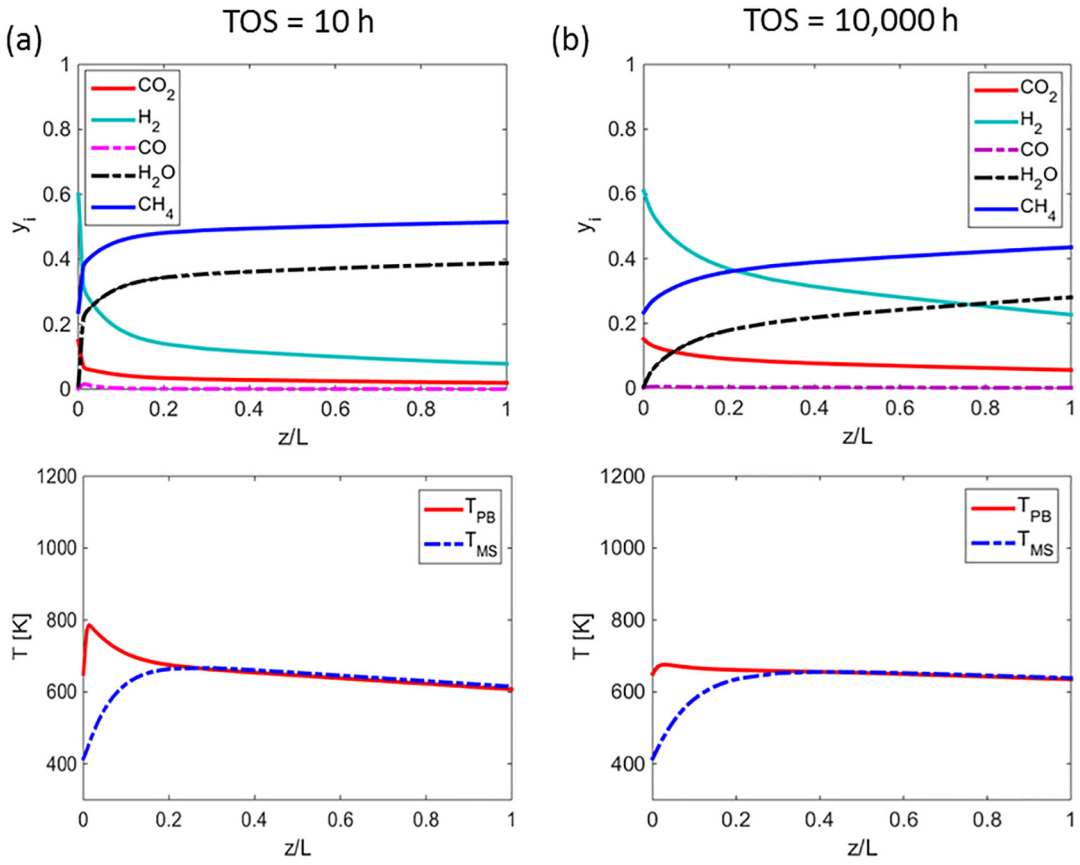

Fig. 4. Spatial profiles of mole fractions (upper panels) and temperatures (lower panel) for TOS = 10 h (a) and TOS = 10,000 h (b), for the *biogas-fed reactor*. T_{PB} and T_{MS} are temperatures of the packed bed (PB) and molten salt (MS). *Parameters:* T_f = 650 K, *GHSV* = 1000 h^{-1}, P_f = 5 bar, $G_c = 0.4G_{c,0}$.

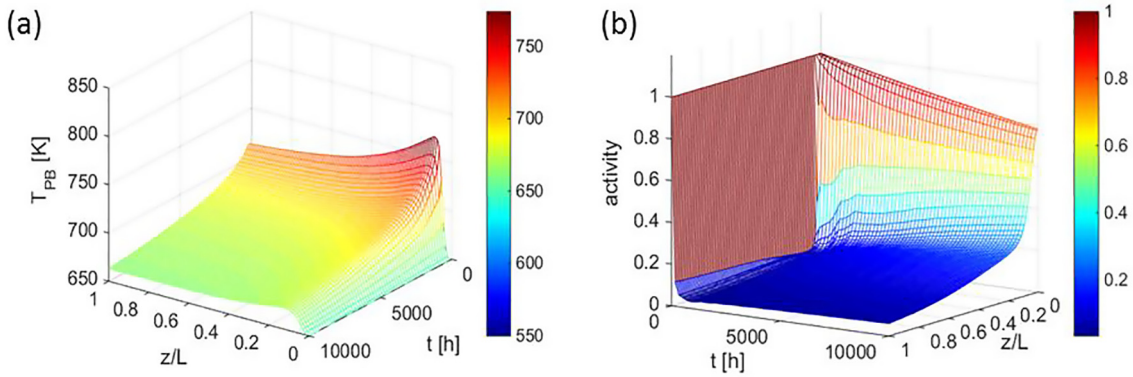

Fig. 5. Spatiotemporal profiles of the packed bed temperature (a) and catalyst activity (b) for the *biogas-fed reactor*. *Parameters:* T_f = 650 K, *GHSV* = 5000 h^{-1}, P_f = 2 bar, $G_c = 0.4G_{c,0}$.

stoichiometric ratio of $H_2/CO_2 = 4$ was kept in all simulations, including biogas feed for which the feed composition in terms of gas molar fractions was 8/13 H_2, 2/13 CO_2, and 3/13 CH_4. All operating parameters are listed in Table 2.

Variable operating parameters include the gas hourly space velocity (GHSV), feed pressure (P_f), and normalized cooling rate ($G_c/G_{c,0}$). Gas hourly space velocity (volumetric feed flow rate divided by the packed bed volume) is defined as follows:

$$GHSV = \frac{\varepsilon v_{gf}}{L} \tag{28}$$

The reference molten salt gravimetric flow rate is calculated assuming that the heat generation rate (for complete CO_2 conversion and no CO formation) is equal to the rate of heat removal by the molten salt (assuming that ΔT_{MS} = 300 K; the operating range of the molten salt is 415–758 K [42]):

$$G_{c,0} = \frac{y_{CO_2}\Delta H_{SR}F_{tf}}{C_{pc}\Delta T_{MS}} \quad F_{tf} = \rho_{gf}V_{PB}GHSV \tag{29}$$

3.1. Catalyst deactivation effect: Reactor fed with pure CO_2 and H_2

Spatial profiles of mole fractions and temperatures in the packed bed and cooling (molten salt) compartments for TOS = 10 h and TOS = 10,000 h are shown in Fig. 2; TOS stands for time on

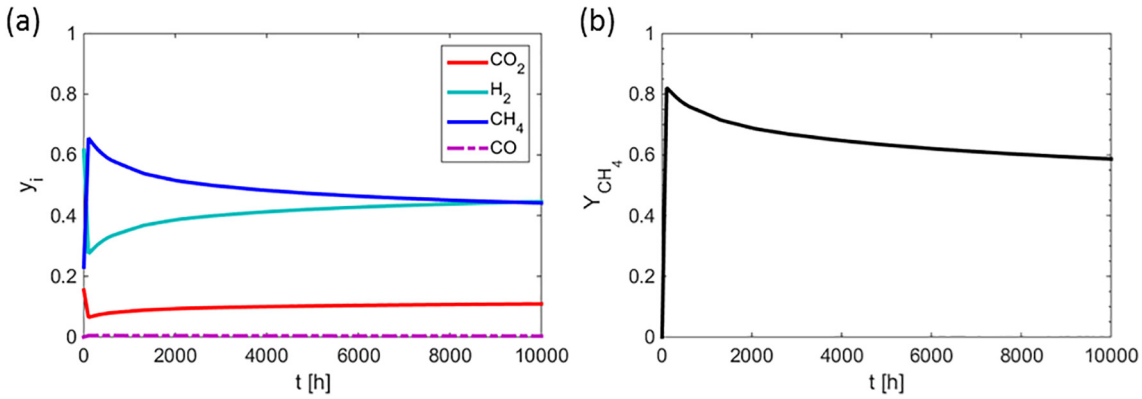

Fig. 6. Temporal evolution of the reactor outlet composition as dry basis mole fractions (a) and CH_4 yield, Eq. (27a) (b) for the *biogas-fed reactor*. *Parameters:* T_f = 650 K, *GHSV* = 5000 h^{-1}, P_f = 2 bar, $G_c = 0.4G_{c,0}$.

Table 2
Operating conditions.

H_2/CO_2	T_f [K]	T_{cf} [K]	$G_c/G_{c,0}$	P_f [bar]	GHSV [h^{-1}]	TOS [h]
4/1	650–700	415	0.08–0.77	1–20	1000–25,000	10–10,000

H_2/CO_2 denotes the ratio of feed mole fraction of H_2 to CO_2; T_f and T_{cf} stand for the feed temperature of reactants and coolant. Variable parameters are the normalized molten salt flow rate ($G_c/G_{c,0}$), feed pressure (P_f), space velocity (GHSV), and time-on-stream (TOS).

stream. At TOS = 10 h, Fig.2a, the simulation predicts that reactions mainly take place in the vicinity of the reactor entrance as it is evident from sharp consumption of H_2 and CO_2 accompanied by a spike in the temperature profile.

The hot spot is formed at the reactor entrance and the difference between the temperatures in the packed bed and molten salt compartments is significant, indicating that the rate of heat generation is significantly higher than the rate of inter-compartment heat transfer. For z/L > 0.4, nearly same temperatures are obtained in the packed bed and molten salt compartments. A small difference in the outlet temperatures (slightly lower for the packed bed) is because of heat losses to the environment, Eq. (8). The outlet stream contains mainly H_2O and CH_4, alongside with a relatively small fractions of H_2 and CO_2, upper panel in Fig. 2a. A small amount of CO, which is formed at the hot spot, is consumed downstream the reactor via either water gas shift or CO methanation, Eqs. (1), (2).

After TOS = 10,000 h, very different spatial profiles are formed, Fig.2b, which can be attributed to catalyst deactivation. This observation emphasizes the importance of performing dynamic simulations that account for the temporal decay of catalyst activity, Eqs. (7), (8), as opposed to steady state simulations. By analyzing spatial profiles at TOS = 10,000 h one can conclude that the catalyst deactivation affects the reactor performance very significantly: no CO formed and the reactions take place over the entire catalytic bed, gradually consuming H_2 and CO_2. As a result, even though much less CO_2 is converted in the vicinity of the reactor entrance, CH_4 production only drops by less than 30%, as it can be deduced from analyzing outlet CH_4 fractions (compare upper panels in Fig.2a and b). The effect of catalyst deactivation is also evident from comparing the temperature profiles in the packed bed at TOS = 10 and 10,000 h, Fig. 2. Lower maximum temperature at TOS = 10,000 h can be attributed to the lower catalyst activity resulting in less heat generation.

Temporal evolution of the reactor performance at elevated space velocity (GHSV = 25,000 h^{-1}) is analyzed in Fig. 3. The effect of catalyst deactivation is clearly observable in Fig. 2a: CO_2 conversion and CH_4 yield decline significantly over time (shown in log scale). Note that X_{CO_2} and Y_{CH_4} shown in this plot are calculated at the reactor outlet (z/L = 1). Similar to the case of GHSV = 1000 h^{-1} (Fig. 2), CO content in the outlet stream is negligible, as it can be seen from the nearly complete selectivity to CH_4, Fig. 3a. The absence of significant amounts of CO can be attributed to the relatively low reactor temperature, Fig. 2b, which is achieved due to the active heat removal via the multiple molten salt tubes, Fig. 1. There is still a hot spot formation, but its temperature decreases over the course of time, Fig. 2b.

The decrease of temperature is due to catalyst deactivation that results in significantly lower reaction rates, Fig. 3c. The reaction mainly takes place at the location of the hot spot, which is expected due to the mutual dependence of reaction and heat generation rates: lower reaction rates results in less heat generation and otherwise. The catalyst remains fully active at the reactor entrance due to the high concentration of H_2 in the reactor feed, Eqs. (18), (19). However, as the reaction takes place, Fig. 3c, the catalyst activity drops sharply forming a steep front, Fig. 3d. Downstream the reactor, there is certain recovery in the catalyst activity due to the lower temperature; recall the exponential dependence of the deactivation rate on temperature Eqs. (18), (19). The initial sharp decay in activity in almost the entire reactor, Fig. 3d, is associated with the highly nonlinear (exponential) dependence of the catalyst activity on time, Eq. (18). To interpret the mathematical formulation, less active sites remain available for the reaction as a result of the catalyst deactivation, slowing down the reaction rate. The decline in the reaction rate slows down the rate of deactivation resulting in stabilization, Fig. 3d.

In summary, the effect of catalyst deactivation is clearly observable in our model. Note that since we assumed catalyst coking as the only mechanism for catalyst deactivation, Eqs. (17)–(19), the catalyst activity profile in Fig. 3d reversely coincide with the normalized carbon deposition profile (carbon deposited normalized by the maximum possible deposited carbon amount). If the catalyst is fully active, there will be no carbon deposited, if the activity is very low, the catalyst surface will be almost completely covered by carbon. The deactivation time scale is relatively long for the operating parameters used in the simulations (Table 2) and for the adopted deactivation rate expression, Eq. (19). Importantly, though the catalyst is almost fully deactivated in the vicinity of the hot spot, Fig. 3d, there is a small region at the reactor entrance where the activity remains almost complete due to the high

concentration of H_2 in the reactor feed. As a result, the reaction still takes place, though at a significantly lower rate, Fig. 3c. For long operation times, the activity and reaction profiles are stabilizing and the reactor still operates at ~55% CH_4 yield after 10,000 h TOS. Still, the reactor performance drops by ~30% due to the catalyst deactivation, Fig. 3a.

3.2. Reactor fed with biogas

In this section, reactor fed with biogas (60% CH_4, 40% CO_2) is investigated, assuming that catalyst-poisoning impurities and water were removed from the feed stream. See Table 2 and related description for details on parameters used in the simulations. All results presented in Section 3.2 were obtained with the simulated biogas feed; the CH_4 yield is calculated using Eq. (27a). Typical profiles are shown in Fig. 4, for short-term operation (TOS = 10 h) and for the extended time on stream (TOS = 10,000 h). The obtained spatial distributions are quite different from those obtained with the pure CO_2 feed, Fig. 2. One of the most noticeable distinctions is the significantly lower temperature of the hot spot (lower panels in Fig. 4).

In principle, lower temperatures could result from the endothermic steam reforming reactions, right-to-left in Eqs. (1), (3), i.e. CH_4 reacting with H_2O produced in the methanation reaction. However, from the analysis of the spatial profiles (upper panels in Fig. 4) it can be concluded that the lower temperature is rather the result of lower CO_2 concentration (dilution) imposed by the use of the biogas feed and 1/4 CO_2/H_2 stoichiometry. These constrains result in the CO_2 feed concentration of 2/13, as opposed to 1/5 for the case of pure CO_2 feed.

For TOS = 10 h, the simulation predicts that the outlet stream is composed of mainly CH_4 and water, also containing less than 10% of H_2 and a small fraction of unreacted CO_2. After 10,000 h on stream, CO_2 conversion drops significantly, as it is evident from higher CO_2 and H_2 fractions in the outlet stream, Fig.4b. Similar to Fig. 2, this change is attributed to the catalyst deactivation, as it can be also seen from the disappearance of the hot spot near the reactor entrance, lower panel in Fig.4b. While for the short operation time most of H_2 and CO_2 are consumed in the first third of the reactor (upper panel in Fig.4a), reactant consumption is more distributed after 10,000 h on stream, (upper panel in Fig.4b).

Spatiotemporal profiles of the reaction compartment temperature and catalyst activity for higher space velocity (GHSV = 5000 h^{-1}) are shown in Fig. 5. The temperature distribution is qualitatively similar to that obtained with the pure CO_2 feed, Fig. 3b, though significantly lower temperatures are obtained. The activity profile, on the other hand, is qualitatively different; compare Fig. 5b with Fig. 3d. First of all, for the case of the biogas feed there is a decline of the catalyst activity at the reactor entrance, which can be attributed to the presence of a significant fraction of CH_4 in the feed. The sharp front at the reactor entrance is still formed. Second, while the activity declines at the inlet, it steadily increases in the entire catalytic bed over the course of time.

This can be explained by the mutual feedbacks between the reaction rate, the rate of heat generation, and catalyst deactivation rate. As the catalyst is being deactivated, the reaction rate decreases, resulting in lower temperatures. Lower temperatures result in a slower reaction rate, less CH_4 production and, therefore, slower deactivation. This interplay eventually slows down the process of catalyst deactivation, leading to the recovery and stabilization of the catalyst activity profile. These finding emphasize the importance of the use of dynamic models for the design of reactors that involve catalytic systems susceptible to deactivation.

For practical application, it will be important to identify the composition of the outlet stream over the course of the reactor operation. Water can be easily condensed downstream the methanation reactor and the product stream is expected to contain CO_2, CH_4, CO and H_2. Representative profiles (on dry basis) are shown in Fig. 6 (same operating conditions as in Fig. 5). In the beginning of the reactor operation the simulation predicts the product stream composed of ~65% CH_4, ~30% H_2, ~5% CO_2, and negligible fraction of CO. Depending on downstream application, H_2 might need to be removed from the outlet stream, but the CO_2 concentration is low. Because of the catalyst deactivation the outlet composition gradually changes, resulting in ~45% CH_4 and H_2, and slightly above 10% of CO_2. The CH_4 yield, Eq. (27a) is above 80% in the beginning, but declines to below 60% after 10,000 h on stream, Fig. 6b. To sum up, the model predicts that reasonably high CO_2 conversions and CH_4 yields are obtainable in the molten salt-cooled packed bed reactor fed with raw biogas (after Sulphur removal).

3.2.1. Effect of space velocity

It is highly desirable to operate at high space velocities in order to maximize the reactor throughput. However, high space velocities typically result in lower conversions (because of low residence times) and, in some case, can result in reactor overcooling, causing extinction. Higher rates of CH_4 production will also accelerate catalyst deactivation. Therefore, it is of crucial importance to determine reactor performance over the wide range of space velocities. In Fig. 7, the reactor performance is evaluated as a function of space velocity for different operation times.

At low space velocities (GHSV < 5000 h^{-1}), CH_4 yields up to 95% are predicted in the beginning of operation, declining to 60–80% yield after 10,000 h on stream, Fig. 7a. In fact, operating at GHSV = 1000 h^{-1} (residence time less than 5 s) allows obtaining CH_4 yield in the 80–95% range over the 10,000 h operation period. As the reactor throughput is increased beyond GHSV = 5000 h^{-1}, the reactor performance continues to decline, still allowing working in the 50–80% CH_4 yield range. Above GHSV = 20,000 h^{-1}, CH_4 production rate drops sharply.

The effect of the catalyst deactivation is apparent from the observation of temporal evolution, Fig. 7b. At low space velocity (1000 h^{-1}), when CH_4 production rate is relatively low, catalyst deactivation is slow, losing only ~15% of CH_4 yield over the course of 10,000 h. For GHSV = 10,000 h^{-1}, the CH_4 yield is lower from the beginning which can be attributed to kinetic limitations (shorter residence times, less than 1 s). The slope of the decay is similar to that obtained with GHSV = 1000 h^{-1}. For GHSV = 20,000 h^{-1}, the starting CH_4 yield is still above 60%, but the decay slope is much sharper. For GHSV = 25,000 h^{-1}, the decay is slow, but it is attributed to very low CO_2 conversion; under these conditions the reactor is clearly limited kinetically or/and overcooled. Since in all simulations the feed temperature was 650 K or higher, the overcooling should be attributed with the heat removal by the molten salt (discussed in more detail in Section 3.2.3).

3.2.2. Effect of pressure

Using raw biogas as a feed could be an attractive alternative to the use of pure CO_2 as a feedstock, since it does not require costly CO_2 separation; gas clean-up to remove H_2S will be still required. However, raw biogas contains a high fraction of CH_4 (~60%) which can cause catalyst deactivation immediately at the reactor entrance due to the high partial pressure of CH_4 accompanied by the high feed temperature, Eq. (19). High operating pressures will result in high CH_4 partial pressures over the entire catalytic bed affecting the catalyst deactivation rate. On the other hand, in many cases it is beneficial to run a process at elevated pressures to maximize the process throughput. The effect of the operating pressure on the reactor performance is investigated in this section.

Fig. 8 demonstrates the effect of feed pressure on the CH_4 yield at GHSV = 10,000 h^{-1}, Fig. 8a, showing also corresponding catalyst activity profiles obtained at TOS = 10,000 h, Fig.8b. It can be seen

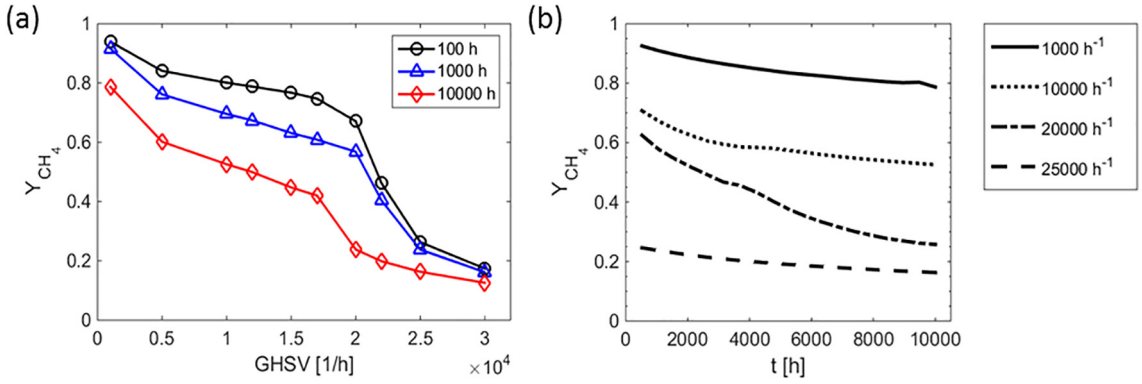

Fig. 7. Effect of space velocity on the reactor performance for the *biogas-fed reactor*: CH_4 yield, Eq. (27a), versus GHSV for TOS = 100, 1000, and 10,000 h (a) and temporal evolution for GHSV = 1000, 10,000, 20,000, 25,000 h^{-1} (b). *Parameters:* T_f = 650 K, P_f = 2 bar, $G_c = 0.4G_{c,0}$.

that increasing the feed pressure initially results in a relatively small decrease in the CH_4 yield, Fig. 8a. This is apparently in contradiction with the Sabatier reaction equilibrium that predicts higher CO_2 conversions for increasing pressures since there is a decrease in number of moles, Eq. (3); pressure drop, Eq. (12), was negligible.

However, high pressures are expected to accelerate catalyst deactivation. Indeed, it can be seen from Fig. 8a that not only the initial CH_4 yield but also the rate of its decline are higher for higher pressures, indicating that catalyst deactivation plays role in poor reactor performance at high pressures. Examining the catalyst activity profiles at TOS = 10,000 h, Fig. 8b, shows an interesting trend; the activity actually increases with pressure, except for the small region in the vicinity of the reactor inlet.

These results can be interpreted by examining the spatiotemporal profiles of the catalytic bed temperature and catalyst activity, Fig. 9 (for P_f = 10 bar). Strong catalyst deactivation at the reactor entrance is evident, as it is expected for the reactor fed with biogas. Since the rate of this deactivation is pressure dependent, Eq. (19), the decay of the catalyst activity and, therefore, of the CH_4 yield is expected to be faster for higher pressures, as it is observed in Fig. 8a. The catalyst deactivation also results in the temperature

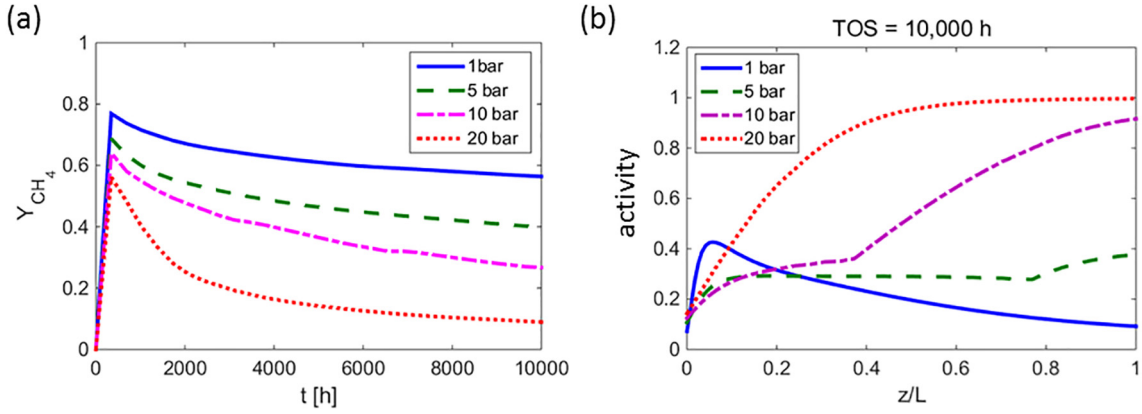

Fig. 8. Effect of feed pressure on methane yield (a), and spatial profiles of catalyst activity for TOS = 10,000 h (b), for the *biogas-fed reactor*. *Parameters:* T_f = 700 K, *GHSV* = 10,000 h^{-1}, $G_c = 0.4G_{c,0}$.

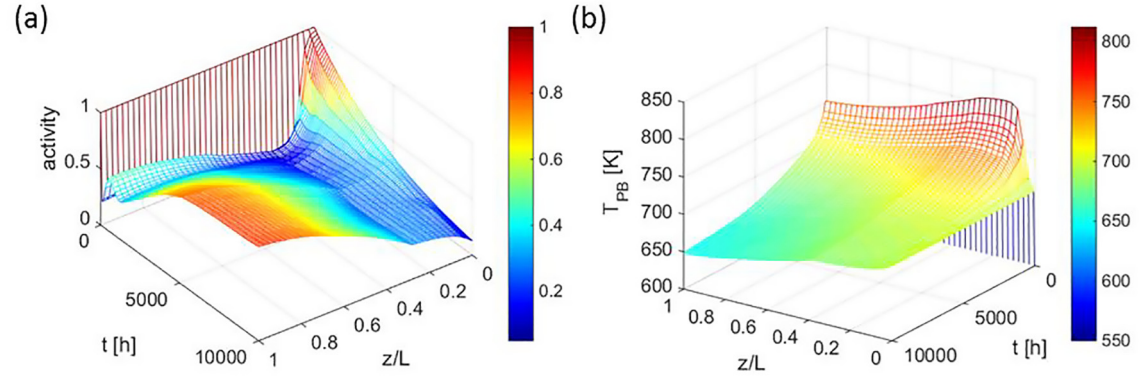

Fig. 9. Spatiotemporal profiles of catalyst activity (a) and packed bed temperature (b) for the *biogas-fed reactor*. *Parameters:* T_f = 700 K, P_f = 10 bar, *GHSV* = 10,000 h^{-1}, $G_c = 0.4G_{c,0}$.

decrease, Fig. 9b. Eventually, the temperature near the reactor entrance is almost equal to the feed temperature, meaning that no ignition occurs. The bed temperature gradually decreases downstream the reactor due to the heat removal by the molten salt cooling tubes, eventually resulting in temperatures below 700 K. These temperatures are too low to obtain high conversion. The reason for the high catalyst activity in the second half of the reactor, Fig. 9a, is that the temperature is relatively low there resulting in a low rate of the CH_4 cracking and coking, Eq. (19). To sum up, increasing operating pressure is not necessary a good strategy for the reactor fed with biogas, because of high CH_4 content in the feed and accelerated rate of catalyst deactivation induced by high partial pressures of CH_4.

3.2.3. Effect of cooling rate

Efficient heat removal is of vital importance for the operation of the highly exothermic Sabatier reactor, but it can also affect the catalyst activity indirectly. Heat removal decreases the reactor

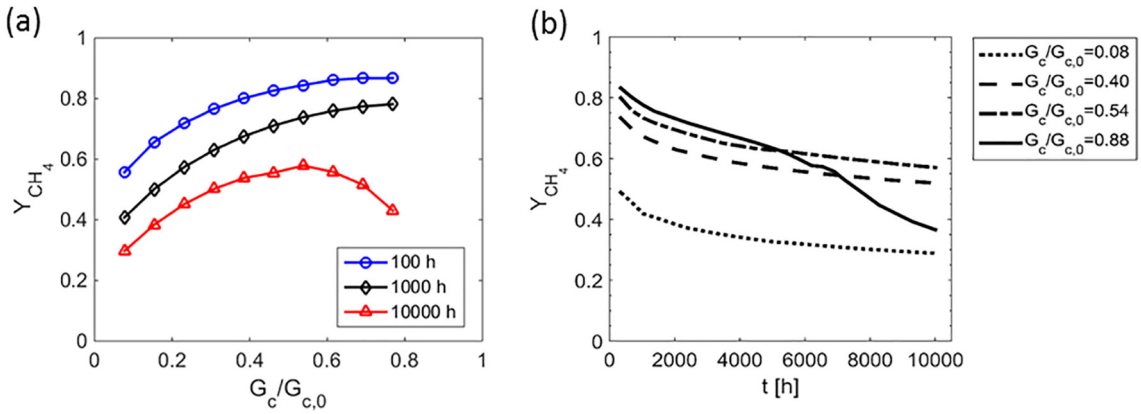

Fig. 10. Reactor performance versus heat removal rate: CH_4 yield, Eq. (27a), as a function of the normalized molten salt flow rate, Eq. (29), for TOS = 100, 1000, and 10,000 h (a) and temporal evolution for $G_c/G_{c,0}$ = 0.08, 0.40, 0.54, and 0.88 (b); for the *biogas-fed reactor*. *Parameters:* T_f = 650 K, P_f = 2 bar, *GHSV* = 10,000 h^{-1}.

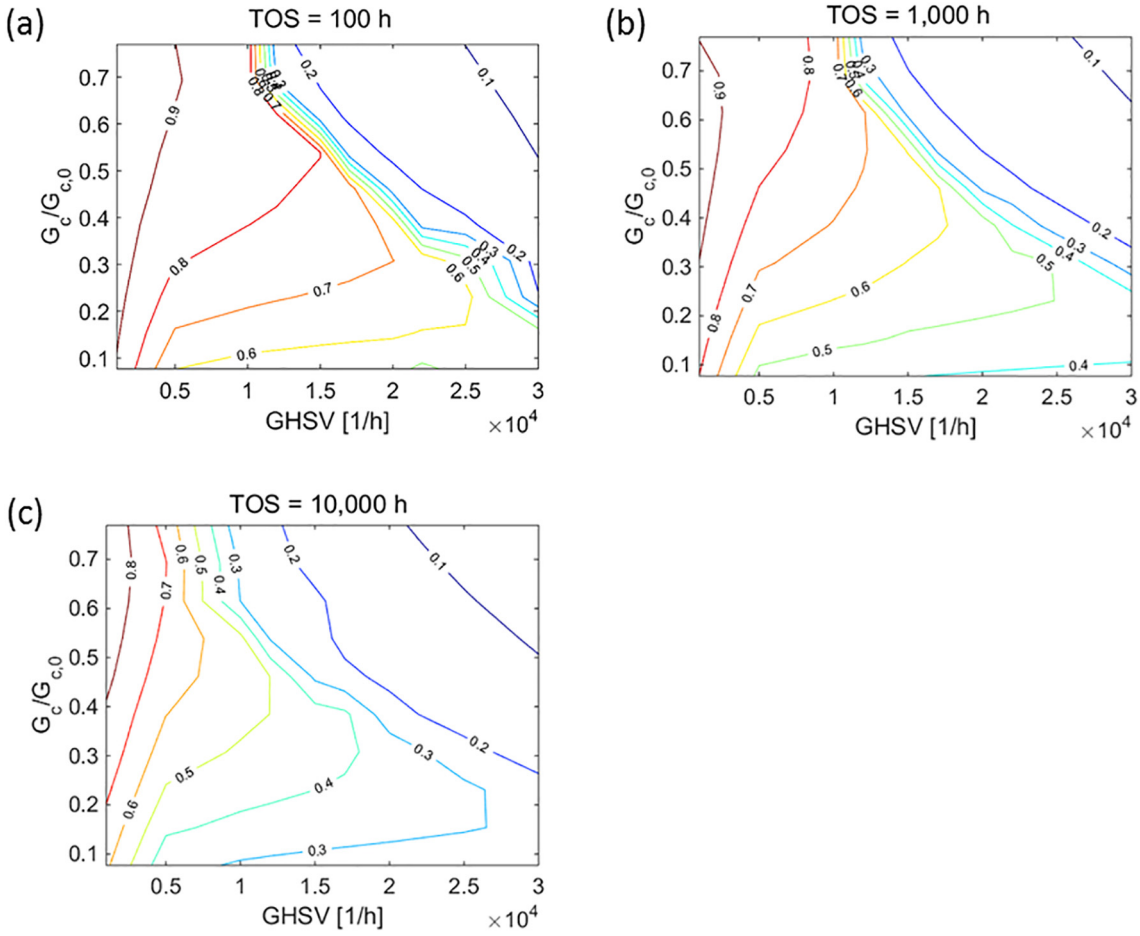

Fig. 11. Reactor performance for the *biogas-fed reactor* in terms of CH_4 yield, Eq. (27a) in the 2D operation domain of reactor throughput (GHSV) and heat removal rate ($G_c/G_{c,0}$) for TOS = 100 h (a), 1000 h (b), and 10,000 h (c). *Fixed parameters:* T_f = 650 K, P_f = 2 bar.

temperature favoring CH_4 production according to the thermodynamic equilibrium, since the Sabatier reaction is highly exothermic, Eq. (3). However, increased CH_4 production can potentially lead to faster catalyst deactivation due to CH_4 cracking and coking of the catalyst surface. In all simulations results shown until this point, the cooling rate was set to an intermediate value of $G_c = 0.4\text{-}G_{c,0}$; $G_{c,0}$ is defined by Eq. (29). In this section, the effect of the cooling rate on the reactor performance is investigated.

In Fig. 10, the reactor performance is evaluated in terms of CH_4 yield, Eq. (27a), as a function of the normalized cooling rate, $G_c/G_{c,0}$, Eq. (29). It can be seen that increasing the cooling rate promotes CH_4 production due to the more efficient heat removal, Fig. 10a. The improvement is very significant, ranging from 60 to 90% over the course of the 1000 h operation period. However, for extended operation (TOS = 10,000 h) the increase of the cooling rate above $G_C/G_{C,0} = 0.54$ actually reduces the CH_4 production, resulting in a distinct optimum, Fig. 10a. This finding can be attributed to the effect of catalyst deactivation that is accelerated at higher CH_4 production rates. It is also evident from the examination of the temporal evolution, Fig. 10b. For $G_C/G_{C,0} = 0.88$, the decay rate is initially similar to those obtained with slower cooling, but after approximately 5000 h TOS, the slope changes and the deactivation becomes rapid. This finding indicates again the importance of the use of dynamic modeling for catalytic systems subject to deactivation.

3.2.4. Optimization of heat removal and reactor throughput

The existence of the catalyst deactivation makes the problem of the reactor performance optimization rather complicated, since optimal conditions could change during the course of reactor operation. The two important parameters, which and relatively easily adjustable in a practical situation, are the space velocity (reactor throughput) and the molten salt flow rate (cooling rate). In this section, the reactor performance in terms of CH_4 yield is optimized using a dynamic scan over the 2D operational window of the cooling rate vs. space velocity, Fig. 11.

The analysis of the obtained maps shows that obtaining 80–90% CH_4 yields over extended periods of continuous operation should be possible. For that, the reactor should be operated below GHSV = 5000 h^{-1} and above $G_c/G_{c,0} = 0.5$. For short-term operation, it is possible to operate at elevated space velocities, with cooling rates ranging from $G_c/G_{c,0} = 0.3\text{–}0.6$. The short-term operation strategy is in principle possible if there is a possibility of periodic regeneration of the catalytic bed. For intermediate space velocities ranging from GHSV = 10,000–20,000 h^{-1}, there are distinct maxima in the CH_4 yield versus cooling rate.

Generally speaking, analysis of such maps can determine the operation window where the maximal CH_4 yield can be obtained over a certain period of operation. Depending on demand, various strategies can be implemented. For example, a certain domain where initially the CH_4 yield is very high but decays significantly at 10,000 h can be selected for short-term operation. For extended operation times, it is beneficial to select a domain where the CH_4 yield is maintained relatively high over the entire period of operation. The selection can be quantitatively constrained by maximizing the overall CH_4 production, integrated over the entire period of time. Further investigation is currently underway in order to develop a thorough optimization algorithm.

4. Concluding remarks

A mathematical model of the Sabatier reactor for conversion of CO_2 into synthetic CH_4 was defined and analyzed by numerical simulations. The reactor was a heat-exchanger type packed bed cooled by multiple tubes with flowing molten salt. The model considered inter-compartment heat exchange and catalyst deactivation by coking, assuming the use of the Ni/Al_2O_3 catalyst. The reactor performance was investigated for the case of the feed containing CO_2 and H_2, and for the case of the reactor fed with biogas (40% CO_2 and 60% CH_4) and H_2, in terms of CO_2 conversion and CH_4 yield. The effects of space velocity, operating pressure, and molten salt flow rate on the reactor performance were investigated in detail for the case of the reactor fed with biogas. The CH_4 yield was mapped in the dynamic two-dimensional domain of the two crucial operating parameters: space velocity and cooling rate.

The model predicts that the reactor can be operated with CH_4 yields ranging from 80 to 90% at intermediate space velocities ranging from 1000 to 10,000 h^{-1} for extended periods of operation, up to 10,000 h time on stream. Further increase in reactor throughput results in a sharp decline of the reactor performance mainly due to the kinetic limitations and overcooling. High pressures, which are favorable for CH_4 production according to the equilibrium and beneficial for practical applications, actually causes faster catalyst deactivation due to the higher partial pressure of CH_4, resulting in a poor reactor performance.

The molten salt flow rate, i.e. cooling rate, is a crucial parameter affecting the reactor performance. The model predicts that the CH_4 yield can be improved by 60–90% over short operating periods. For extended, >1000 h time on stream operation, the effect of heat removal is more complicated and distinct maxima in CH_4 production are observed. Scanning the reactor performance over extended ranges of space velocities (reactor throughput) and molten salt flow rates (heat removal rate) shows a non-trivial, dynamically evolving map. An algorithm for the reaction performance evaluation is currently under development.

Acknowledgements

The authors acknowledge the support of the Waterloo Institute of Sustainable Energy (WISE), Ontario, Canada, through the WISE – Cisco Systems Smart Grid Research Fund.

References

[1] W. Wang, S. Wang, X. Ma, J. Gong, Recent advances in catalytic hydrogenation of carbon dioxide, Chem. Soc. Rev. 40 (2011) 3703–3727.
[2] T. Inui, Highly effective conversion of carbon dioxide to valuable compounds on composite catalysts, Catal. Today 29 (1996) 329–337.
[3] G.D. Weatherbee, C.H. Bartholomew, Hydrogenation of CO_2 on group VIII metals: IV. Specific activities and selectivities of silica-supported Co, Fe, and Ru, J. Catal. 87 (1984) 352–362.
[4] Y. Zhang, G. Jacobs, D.E. Sparks, M.E. Dry, B.H. Davis, CO and CO_2 hydrogenation study on supported cobalt Fischer-Tropsch synthesis catalysts, Catal. Today 71 (2002) 411–418.
[5] P.J. Lunde, F.L. Kester, Carbon dioxide methanation on a ruthenium catalyst, Ind. Eng. Chem. Proc. Des. Dev. 13 (1974) 27–33.
[6] K.R. Thampi, J. Kiwi, M. Graetzel, Methanation and photo-methanation of carbon dioxide at room temperature and atmospheric pressure, Nature 327 (1987) 506–508.
[7] F. Solymosi, A. Erdöhelyi, T. Bansagi, Methanation of CO_2 on supported rhodium catalyst, J. Catal. 68 (1981) 371–382.
[8] G.A. Mills, F.W. Steffgen, Catalytic methanation, Catal. Rev. 8 (1974) 159–210.
[9] C. Bartholomew, Catalyst deactivation and regeneration, Kirk-Othmer Encyclopedia of Chemical Technology, 2003.
[10] R. Dalla Betta, A. Piken, M. Shelef, Heterogeneous methanation: steady-state rate of CO hydrogenation on supported ruthenium, nickel and rhenium, J. Catal. 40 (1975) 173–183.
[11] M. Agnelli, M. Kolb, C. Mirodatos, CO hydrogenation on a nickel catalyst.: 1. Kinetics and modeling of a low-temperature sintering process, J. Catal. 148 (1994) 9–21.
[12] M.N. Pedernera, J. Piña, D.O. Borio, Kinetic evaluation of carbon formation in a membrane reactor for methane reforming, Chem. Eng. J. 134 (2007) 138–144.
[13] J.B. Claridge, M.L. Green, S.C. Tsang, A.P. York, A.T. Ashcroft, P.D. Battle, A study of carbon deposition on catalysts during the partial oxidation of methane to synthesis gas, Catal. Lett. 22 (1993) 299–305.
[14] K. Nikooyeh, R. Clemmer, V. Alzate-Restrepo, J.M. Hill, Effect of hydrogen on carbon formation on Ni/YSZ composites exposed to methane, Appl. Catal. A: Gen. 347 (2008) 106–111.

[15] J.-W. Snoeck, G. Froment, M. Fowles, Steam/CO_2 reforming of methane. Carbon filament formation by the Boudouard reaction and gasification by CO_2, by H_2, and by steam: kinetic study, Ind. Eng. Chem. Res. 41 (2002) 4252–4265.
[16] M. Ermakova, D.Y. Ermakov, G. Kuvshinov, L. Plyasova, New nickel catalysts for the formation of filamentous carbon in the reaction of methane decomposition, J. Catal. 187 (1999) 77–84.
[17] J.R. Rostrup-Nielsen, Steam Reforming Catalysts: An Investigation of Catalysts for Tubular Steam Reforming of Hydrocarbons: A Contribution From the Research Laboratory of Haldor Topsøe A/S, Teknisk Forlag, 1975.
[18] D.S.A. Simakov, M. Sheintuch, Model-based optimization of hydrogen generation by methane steam reforming in autothermal packed-bed membrane reformer, AIChE J. 57 (2011) 525–541.
[19] D.S.A. Simakov, M. Sheintuch, Design of a thermally balanced membrane reformer for hydrogen production, AIChE J. 54 (2008) 2735–2750.
[20] M. Borghei, R. Karimzadeh, A. Rashidi, N. Izadi, Kinetics of methane decomposition to COx-free hydrogen and carbon nanofiber over Ni–Cu/MgO catalyst, Int. J. Hydrogen Energy 35 (2010) 9479–9488.
[21] S. Rönsch, J. Schneider, S. Matthischke, M. Schlüter, M. Götz, J. Lefebvre, P. Prabhakaran, S. Bajohr, Review on methanation – from fundamentals to current projects, Fuel 166 (2016) 276–296.
[22] S.A.M. Said, D.S.A. Simakov, M. Waseeuddin, Y. Roman-Leshkov, Solar molten salt heated membrane reformer for natural gas upgrading and hydrogen generation: a CFD model, Solar Energy 124 (2016) 163–176.
[23] B. Hou, Y. Huang, X. Wang, X. Yang, H. Duan, T. Zhang, Optimization and simulation of the Sabatier reaction process in a packed bed, AIChE J. 62 (2016) 2879–2892.
[24] D. Schlereth, O. Hinrichsen, A fixed-bed reactor modeling study on the methanation of CO_2, Chem. Eng. Res. Des. 92 (2014) 702–712.
[25] L. Kiewidt, J. Thöming, Predicting optimal temperature profiles in single-stage fixed-bed reactors for CO_2-methanation, Chem. Eng. Sci. 132 (2015) 59–71.
[26] J. Xu, G.F. Froment, Methane steam reforming, methanation and water-gas shift: I. intrinsic kinetics, AIChE J. 35 (1989) 88–96.
[27] S.S.E.H. Elnashaie, A.M. Adris, A.S. Al-Ubaid, M.A. Soliman, On the non-monotonic behaviour of methane—steam reforming kinetics, Chem. Eng. Sci. 45 (1990) 491–501.
[28] M.L. Rodríguez, M.N. Pedernera, D.O. Borio, Two dimensional modeling of a membrane reactor for ATR of methane, Catal. Today 193 (2012) 137–144.
[29] S. Lee, J.G. Speight, S.K. Loyalka, Gasification of coal, Handbook of Alternative Fuel Technologies, second ed., CRC Press, Boca Raton, FL, 2014.
[30] M.C. Demicheli, E.N. Ponzi, O.A. Ferretti, A.A. Yeramian, Kinetics of carbon formation from CH_4-H_2 mixtures on nickel-alumina catalyst, Chem. Eng. Res. 46 (1991) 129–136.
[31] R.J. Berger, J. Pérez-Ramírez, F. Kapteijn, A. Moulijn, Catalyst performance testing: radial and axial dispersion related to dilution in fixed-bed laboratory reactors, Appl. Catal. A Gen. 227 (2002) 321–333.
[32] A.G. Dixon, D.L. Cresswell, Theoretical prediction of effective heat transfer parameters in packed beds, AIChE J. 25 (1979) 663–676.
[33] O.R. Derkx, A.G. Dixon, Effect of the wall Nusselt number on the simulation of catalytic fixed bed reactors, Catal. Today 35 (1997) 435–442.
[34] O.A. Sergeev, A.G. Shashkov, A.S. Umanskii, Thermophysical properties of quartz glass, J. Eng. Phys. Thermophys. 43 (1982) 1375–1383.
[35] S.W. Churchill, H.H. Chu, Correlating equations for laminar and turbulent free convection from a horizontal cylinder, Int. J. Heat Mass Transfer 18 (1975) 1049–1053.
[36] V. Gnielinski, New equations for heat and mass transfer in turbulent pipe and channel flow, Int. Chem. Eng. 16 (1976) 359–368.
[37] A.F. Mills, Heat Transfer, second ed., Prentice-Hall, New Jersey, 1999.
[38] J.P. Holman, Heat Transfer, ninth ed., McGraw-Hill Inc, New York, Boston, 2002.
[39] G.J. Janz, Molten Salts Handbook, Elsevier, New York, 1967.
[40] Y.S. Touloukian, R.K. Kirby, E.R. Taylor, T.Y.R. Lee, Thermophysical Properties of Matter, Purdue University, The TPRC Data Series, 1977.
[41] R. Morrell, Handbook of Properties of Technical and Engineering Ceramics, Stationery Office Books, London, 1987.
[42] Dynalene Molten Salts, Dynalene, Inc., https://www.dynalene.com/Molten-Salts-s/1831.htm, 2016.
[43] D.S.A. Simakov, M.M. Wright, S. Ahmed, E.M.A. Mokheimer, Y. Román-Leshkov, Solar thermal catalytic reforming of natural gas: a review on chemistry, catalysis and system design, Catal. Sci. Technol. 5 (2015) 1991–2016.